

# Structural and Vibrational Properties of $\text{Al}_2\text{O}_3$ Under Stress

Seung Mi Lee<sup>†</sup>, Nam-Woon Kim<sup>†</sup>, In Young Jung, Chang Soo Kim\*, and Hyunung Yu\*

*Korea Research Institute of Standards and Science, Daejeon 34113, Korea*

We investigated the structural and vibrational properties of strained  $\alpha\text{-Al}_2\text{O}_3$  using experimental measurements of X-ray diffraction and Raman spectroscopy, together with theoretical simulations based on quantum mechanical calculations. Although sapphire has been widely used in industry for display devices, the origin and the effect of residual strain on the structural and the vibrational properties during the fabrication processes were not understood at atomic scale yet. The changes in lattice constants, as measured by high-resolution X-ray diffraction, showed the presence of tensile strain in sapphire during the fabrication. The vibrational properties of  $\alpha\text{-Al}_2\text{O}_3$  have been measured by Raman spectroscopy and the origin of each mode was identified and visualized at the atomic scale with density functional theory simulations. The biaxial tensile strain of  $\alpha\text{-Al}_2\text{O}_3$  affected the vibration modes, resulting in downshifts, as observed by Raman spectroscopy and confirmed by quantum mechanical calculations.

**Keywords:** Sapphire, Strain, Density Functional Theory, X-ray, Raman.

## 1. INTRODUCTION

Over the past few decades, the demand for synthetic sapphire-based materials has tremendously increased due to their potential applications in flat panel displays, medical field, and gem industry. Because of their excellent optical transparency, which is a property required for the light emitting diodes, optical windows of smartphone, and jewellerys, and electronic properties as well as very high resistance to scratch and deformation of sapphire-based materials, much attention has been dedicated to their high-quality fabrication and physical characterization.<sup>1–3</sup>

Sapphire is composed of aluminium and oxygen atoms, forming a corundum structure with hexagonal lattice.<sup>1</sup> Synthetic sapphire crystal is made of high purity over 99.99% alumina powder by slow cooling after melting above 2050 °C. Various routes of crystal growth and fabrication have been studied to produce high purity sapphire.<sup>4,5</sup> Technical requirements to monitor the quality of the purity and crystallinity on the working surfaces of sapphire became more critical because of the sharp increase in the demand for sapphire wafers of large

size.<sup>1,6</sup> Various wafer processes from synthetic sapphire ingot are well-known, however the origin of residual stress is still veiled during ingot growth followed by slicing, lapping, polishing and annealing processes.<sup>5</sup> It also has been demonstrated that the substrate curvature, i.e., bow or even crack during the post process such as epitaxy on the sapphire is a crucial factor for achieving products with high uniformity and with low thickness and large diameter.<sup>1</sup> These originate from the strain on sapphire window for each process and should be overcome by careful investigation analyses to find out the origins.<sup>7,8</sup>

In this study, we report the comparative study performed using experimental measurements and theoretical calculations on strained sapphire ( $\alpha\text{-Al}_2\text{O}_3$ ), with high-resolution X-ray analysis, and Raman spectroscopy, and quantum mechanical calculations, respectively. The changes in the lattice constants were precisely measured using high-resolution X-ray diffractometer (HRXRD) and the vibrational properties were investigated using Raman spectroscopy. The vibrational modes of sapphire were also identified at the atomic scale from the quantum mechanical simulations based on density functional theory calculations; subsequently, the effect of tensile strain on the vibration modes was investigated.

\*Authors to whom correspondence should be addressed.

<sup>†</sup>These two authors contributed equally to this work.

## 2. METHODOLOGY

### 2.1. Experimental

All the sapphire wafers from Sapphire Technology were 99.999% purity and hydrothermal process were carried out in a furnace at 1900 °C for 20 h at a rate of 10 °C/min. We considered five different sampling points at center, top, bottom, and left and right edges of both the front and the back surfaces on the two-inch sapphire wafer.

The lattice constants of the sapphire single crystal wafer were measured using HRXRD on a diffractometer with a 4-bounce Ge (022) monochromator and a 3-bounce Ge (022) analyzer. In order to calculate the lattice constants along the crystallographic *a*-direction, the precise positions of 2θ angles for (006) and (108) reflections were measured for two sapphire wafers, with and without heat treatment at 1900 °C for 10 h.

The vibrational properties were characterized with a confocal Raman microscope (DXR, ThermoFisher Scientific). The sapphire wafer was excited with a 532 nm laser (a high-resolution grating, 2048 pixel array CCD), and the spectra were averaged for 10 s with a 50X objective lens coupled with a 50 μm diameter pinhole.

### 2.2. Theoretical

We performed quantum mechanical calculations within density functional theory (DFT) framework. Atomic orbital basis sets were used as implemented in DMOL3 code<sup>9</sup> in the triple numerical with polarization (TNP) form. All electrons, including those from the core part, were considered during calculations. The exchange-correlation functionals obtained using local density approximation (LDA) and Monkhorst-Pack grid points, at a separation of 0.015/Å, were used. Geometry optimization criteria were 0.005 Å for distance, 0.001 Ha/Å for force, and 10<sup>-5</sup> Ha for total energy.

Vibrational frequencies were computed by diagonalization of the mass-weighted second-derivative Cartesian matrix (i.e., Hessian matrix).<sup>10</sup> The Hessian elements were computed by displacing each atom, and then by computing a gradient vector, thus building up a complete second derivative matrix. In this manner, the vibrational modes were calculated numerically. The Hessian was evaluated using a two-point difference in order to reduce numerical rounding-off errors. Intensities were obtained from the atomic polar tensor, which was a second derivative of the total energy with respect to the Cartesian coordinates and dipole moments. Intensity of each mode was evaluated as a square of all the transition moments of the mode and expressed in terms of the atomic polar tensor matrix and eigenvectors of the mass-weighted Hessian. The displacement step size was 0.005 Å.

## 3. RESULTS AND DISCUSSION

In order to quantify the effect of residual strain on sapphire during fabrication, we measured the structural

and vibrational properties of sapphire using HRXRD and Raman spectroscopy. Figure 1 shows the experimental observations of the sapphire wafers before and after annealing at 1900 °C. Figure 1(A) depicts the change in the lattice constant along the *a*-axis from 4.7586 Å to 4.7590 Å after annealing, as measured by HRXRD. Although the magnitude of change due to the annealing process seems to be insignificant, resolution of the equipment was high enough to show the difference [marked with error bars in Fig. 1(A)]. It is to be noted that from the measurement, the *a*- and *b*-axes of the sample were found to be equivalent. Therefore, the increment in the lattice constant could be interpreted as the tensile stain in the sapphire, which was considered in the quantum mechanical simulation conditions, as would be described later in the section.

The vibrational properties were measured using Raman spectroscopy. Figure 1(B) depicts the full Raman spectra from the wafers before and after annealing. The main peaks of the Raman spectrum of stress-free sapphire (black) were observed at 417.0 and 646.0 cm<sup>-1</sup> (*A*<sub>1g</sub> modes), and at 379.2, 430.4, 449.6, 577.4 and 750.8 cm<sup>-1</sup> (*E*<sub>g</sub> modes), similar to those previously reported values<sup>11</sup> at 417 and

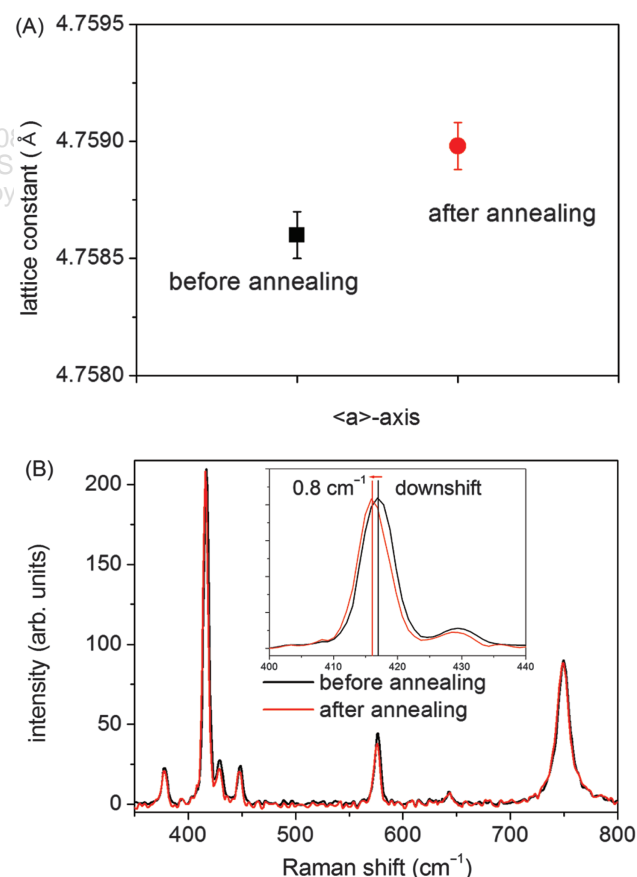


**Figure 1.** Experimental characterization of a sapphire wafer before (black) and after (red) annealing. (A) The variation in lattice constants along the crystallographic *a*-axis, obtained using HRXRD and (B) Raman spectra. The inset of (B) shows the Raman peak with *A*<sub>1g</sub> symmetry at 417.0 cm<sup>-1</sup>.

646 cm<sup>-1</sup> (*A*<sub>1g</sub> modes), and at 379, 431, 450, 578 and 750 cm<sup>-1</sup> (*E*<sub>g</sub> modes). All measured main Raman peaks from the sample after annealing at 1900 °C (red) were found to be at 416.2 and 645.1 cm<sup>-1</sup> (*A*<sub>1g</sub> modes), and at 378.7, 430.1, 448.8, 576.7 and 750.3 cm<sup>-1</sup> (*E*<sub>g</sub> modes). The inset of Figure 1(B) shows the results of Raman shift of the peak at 417.0 cm<sup>-1</sup> by 0.8 cm<sup>-1</sup>. The origin of Raman shift could be point defects such as a vacancy, substitution, interstitial, or dislocations.<sup>12</sup> However, annealing at high temperature, just below the melting point of sapphire, cause straightening of the large number of dislocations in the thin wafer plate.<sup>11</sup> Therefore, we consider that Raman shifts measured in annealed sample mostly originate from the residual tensile, as the HRXRD results also pointed out. The redshift of Raman peaks under tensile strain have been reported in other semiconductors and nanomaterials as well.<sup>13–15</sup> The exploration to other possible origins of Raman shift, such as vacancy or a substitutional defect, is beyond the scope of our current report and may be treated in our next investigation.

We used DFT calculations in order to identify the vibrational modes with/without strain in the atomic scale, and to explain the experimental observations. The DFT calculations have been successfully applied to explain experimental observations, and also to predict the structural, vibrational, and electronic properties.<sup>16–19</sup> Prior to the performing simulations on the sapphire, we conducted several benchmark tests with various exchange-correlation functionals, core-treatments, and basis sets. Optimized bond lengths and the vibrational frequencies obtained from the optimized geometry of diatomic molecules AlO, O<sub>2</sub>, and Al<sub>2</sub>, with various conditions of exchange-correlation functionals and basis sets are summarized in Table I. After series of calculations (Table I), we decided to use the calculation details discussed later in the section, which describes best the vibrational properties of Al–O systems among our calculation conditions. Experimental data<sup>20</sup> are

listed also at the last two columns of Table I for comparison. As can be seen, the bond lengths and vibration frequencies for dimers are in excellent agreement with the experimental values within 2% of difference.

From the calculation details described in the previous paragraph, the theoretical structure parameters were found to be  $a = b = 4.7275$  Å, and  $c = 12.8585$  Å for the lattice constants, and  $\alpha = \beta = 90^\circ$ ,  $\gamma = 120^\circ$  for the bond angles with D<sub>3d</sub><sup>6</sup> symmetry. The optimized atomic geometry of  $\alpha$ -Al<sub>2</sub>O<sub>3</sub> is shown in Figure 2, in polyhedron and ball-and-stick forms. From this optimized geometry, we calculated the vibrational properties in order to identify the vibration modes in atomic scale in the manner as described in the Theoretical section. Using DFT calculations, we were able to verify and visualize the correlation between the atomic movements and vibration frequencies.

As mentioned above, two peaks with *A*<sub>1g</sub> symmetry at 417.0 and 646.0 cm<sup>-1</sup> had high intensity in Raman spectra; therefore, we focused on the *A*<sub>1g</sub> symmetry peaks. The corresponding two modes with *A*<sub>1g</sub> symmetry were found at 423.2 and 643.0 cm<sup>-1</sup> via our DFT calculations. We were able to identify them as stretching modes and the relevant atomic movements are clearly shown in Figure 3. The green arrows indicate the orientations of atomic movements, and the red and the pink balls depict O and Al atoms, respectively. Figures 3(A), (B) show the Al–Al *inter-layer* stretching mode along the *c*-axis, calculated to be at 423.2 cm<sup>-1</sup> (vibration frequency). The O–O *intra-layer* stretching mode in the *a*–*b* plane was found at 643.0 cm<sup>-1</sup>, as shown in Figures 3(C), (D). It is to be noted that the Al–Al or O–O atoms related in the stretching modes were not directly bonded but were present at the 2nd nearest neighbors in both cases, therefore we named them as *inter-* and *intra-layer* stretching, respectively. Other five modes with *E*<sub>g</sub> symmetry were observed to be at 375.4, 431.2, 448.8, 579.0, and 755.7 cm<sup>-1</sup>, and their atomic movements were found to be complex mixture

**Table I.** Optimized bond length and the vibrational frequencies of stretching mode obtained using the optimized geometry of the diatomic molecules, AlO, O<sub>2</sub>, and Al<sub>2</sub>, with various conditions of exchange-correlation functionals (XCs) and basis sets (BSs). Experimental data<sup>20</sup> are listed for comparison in the last two columns.

Molecule	Method		Theory (DFT)		Experiment <sup>20</sup>	
	XC	BS	Bond length (Å)	Frequency (cm <sup>-1</sup> )	Bond length (Å)	Frequency (cm <sup>-1</sup> )
AlO	GGA-PBE <sup>(a)</sup>	DNP <sup>(b)</sup>	1.643	964.13	1.6176	979.23
		DNP+ <sup>(c)</sup>	1.634	959.14		
	GGA-rPBE <sup>(d)</sup>	TNP	1.635	952.30		
		DNP	1.651	947.56		
	GGA-PW91 <sup>(e)</sup>	DNP	1.641	967.22		
	LDA-VWN <sup>(f)</sup>	TNP	1.615	1000.89		
	LDA-PWC <sup>(g)</sup>	DNP	1.624	1002.71		
		DNP+	1.615	1002.60		
O <sub>2</sub>	LDA-PWC <sup>(g)</sup>	TNP	1.615	999.93	1.20752	1580.19
		TNP	1.208	1600.30		
Al <sub>2</sub>	LDA-PWC <sup>(g)</sup>	TNP	2.452	351.31	2.466	350.01

Notes: <sup>(a)</sup>J. P. Perdew, K. Burke, and M. Ernzerhof, *Phys. Rev. Lett.* 77, 3865 (1996). <sup>(b)</sup>Double numeric with polarization. <sup>(c)</sup>DNP with additional diffuse functions. <sup>(d)</sup>B. Hammer, L. B. Hansen, and J. K. Nørskov, *Phys. Rev. B* 59, 7413 (1999). <sup>(e)</sup>J. P. Perdew, J. A. Chevary, S. H. Vosko, K. A. Jackson, M. R. Pederson, and D. J. Somph, *Phys. Rev. B* 46, 6671 (1992). <sup>(f)</sup>S. H. Vosko, L. Wilk, and M. Nusair, *Can. J. Phys.* 58, 1200 (1980). <sup>(g)</sup>J. P. Perdew and Y. Wang, *Phys. Rev. B* 45, 13244 (1992).

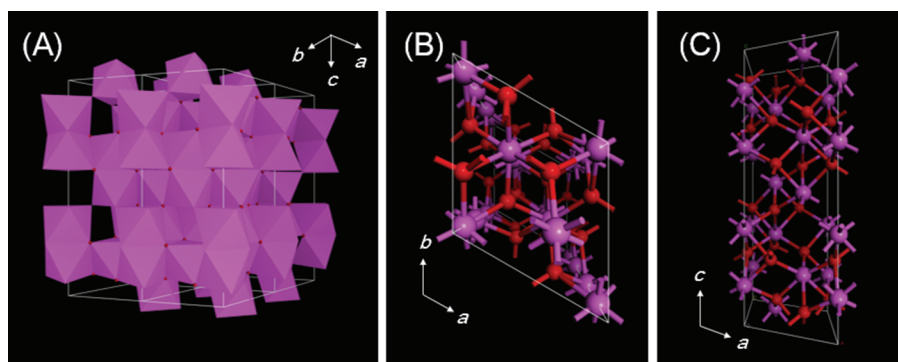


**Figure 2.** The optimized atomic geometry of  $\text{Al}_2\text{O}_3$  corundum in (A) polyhedron and (B)–(C) the ball-and-stick forms. Red balls indicate oxygen atoms while pink balls represent aluminum atoms. White arrows depict the lattice vectors.

of bond bendings and stretchings via our DFT calculations. Compared to the Raman measurements of 417.0 and 646.0  $\text{cm}^{-1}$  for  $A_{1g}$  symmetry and 379.2, 430.4, 449.6, 577.4, and 750.8 for  $E_g$  symmetry, the theoretically calculated peak positions of 423.2 and 643.0  $\text{cm}^{-1}$  for  $A_{1g}$  and for 375.4, 431.2, 448.8, 579.0, and 755.7  $\text{cm}^{-1}$  for  $E_g$  symmetry were slightly underestimated but still in good agreement, as listed in Table II.

In addition, we investigated the vibrational property under tensile strain in plane. We changed the lattice

constants to  $a = b = 4.7417 \text{ \AA}$  in order to mimic the 0.3% of biaxial tensile strain. By repeating the same procedure described in one of the previous paragraphs, we obtained vibrational frequencies and identified vibrational modes from atomic movements. We found that the peak related to the Al–Al *inter-layer* stretching mode along the *c*-axis was shifted from 423.2  $\text{cm}^{-1}$  to 421.9  $\text{cm}^{-1}$ , and that originating from the O–O *intra-layer* stretching mode was shifted much from 643.0  $\text{cm}^{-1}$  to 636.4  $\text{cm}^{-1}$ . The relatively significant downshift in the latter case is attributed to the corresponding atomic movements in the *a*–*b* plane, where the tensile strain had been applied. Under stronger tensile strain of 3%, i.e.,  $a = b = 4.8693 \text{ \AA}$ , resulted in stronger shift of 413.7  $\text{cm}^{-1}$  and 582.7  $\text{cm}^{-1}$  by our simulations. The tendency of downshift of the peak positions under tensile strain was also observed in the Raman spectroscopy measurements, as discussed in previous section.

The symmetric vibrational peak positions of  $\alpha\text{-Al}_2\text{O}_3$  were summarized in the Table II. The first two columns show experimentally observed data of Raman spectroscopy, and the last three columns show the theoretical values obtained using DFT calculations with/without tensile strain. In both the methods, we found the same tendency of downshift of the peaks under biaxial tensile strain. Comparing the peak shifts under two different tensile strains in DFT calculations, the downshifts were more

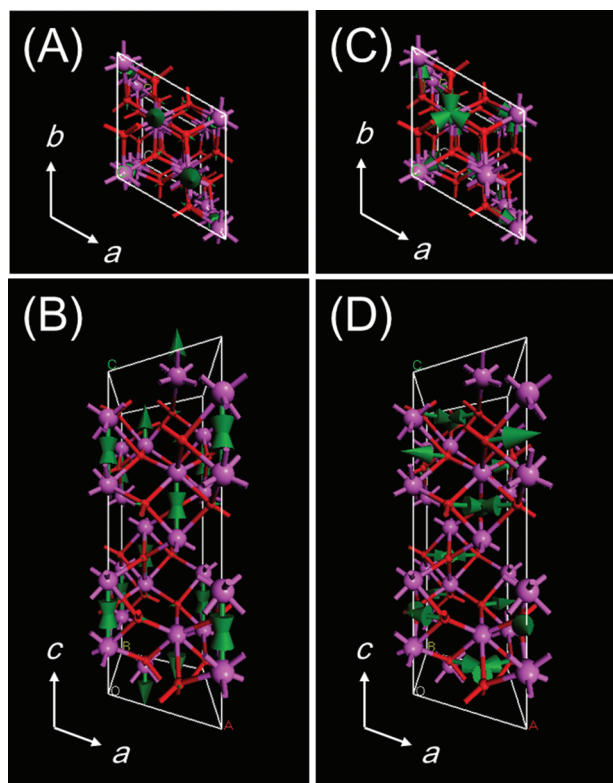


**Figure 3.** The atomic geometries with the schematic atomic movements corresponding to the stretching modes with  $A_{1g}$  symmetry at (A)–(B) 423.2  $\text{cm}^{-1}$  and (C)–(D) 643.0  $\text{cm}^{-1}$  by DFT calculations. Red balls show O atoms, pink balls represent the Al atoms and green arrows depict the direction of the atomic movements. Small white arrows at left bottom show the lattice vectors.

**Table II.** The symmetric vibrational peak positions (in  $\text{cm}^{-1}$ ) of  $\alpha\text{-Al}_2\text{O}_3$  without/with biaxial tensile strain obtained from Raman measurements and DFT calculations.

Methodology symmetry	Experiment (Raman)		Theory (DFT)		
	Strain free	Tensile strain	Strain free	Tensile strain (0.3%)	Tensile strain (3%)
$E_g$	379.2	378.7	375.4	375.0	360.6
$A_{1g}$	417.0	416.2	423.2	421.9	413.7
$E_g$	430.4	430.1	431.2	429.8	413.1
$E_g$	449.6	448.8	448.8	445.4	422.3
$E_g$	577.4	576.7	579.0	573.7	531.0
$A_{1g}$	646.0	645.1	643.0	636.4	582.7
$E_g$	750.8	750.3	755.7	748.8	690.4

significant under higher strain. Our simulated values shows stronger downshifts, which partially due to the relatively large amount of the strain of 0.3% compared to the experimental data. However, we believe that our comparative analysis of the experimental and computational results is still meaningful, showing the same tendency of the downshift of the peak positions.

#### 4. CONCLUSION

We studied the residual tensile strain of sapphire in the fabrication process by experimental measurements using HRXRD and Raman spectroscopy, and theoretical calculations using DFT. The origin of symmetric peaks in Raman spectra has been identified as atomic vibration modes by DFT simulations and the changes of modes have been calculated as increasing the amount of tensile strain. The biaxial tensile strain of  $\alpha$ -Al<sub>2</sub>O<sub>3</sub> affected on its vibration modes, resulting in downshifts, as observed by Raman spectroscopy measurements and confirmed by DFT calculations. Our investigation would help to estimate and overcome the residual strain of large area sapphire in device fabrications.

**Acknowledgments:** The research was supported by Nano-Materials Technology Development Program of the NRF of Korea funded by MEST (NRF-2016M3A7B4025406).

#### References and Notes

1. E. R. Dobrovinskaya, L. A. Lytvynov, and V. Pishchik, *Sapphire*, Springer, New York, USA (2009).
2. H. Aida, H. Takeda, N. Aota, and K. Koyama, *Jap. J. Appl. Phys.* 15, 016504 (2012).
3. M. Kadleikova, J. Breza, and M. Vasely, *Microelectron. J.* 32, 955 (2001).
4. R. W. Cumberland, M. B. Weinberger, J. J. Gilman, S. M. Clark, S. H. Tolbert, and R. B. Kaner, *J. Am. Chem. Soc.* 127, 7264 (2005).
5. H. Tang, H. Li, and L. Xu, *Advanced Topics on Crystal Growth*, InTech Press, Rijeka, Croatia (2013), pp. 302–332.
6. C. P. Khattak and F. Schmid, *J. Cryst. Growth* 225, 572 (2001).
7. V. A. Coleman, J. E. Bradly, C. Jagadish, P. Munroe, Y. W. Heo, S. J. Pearton, D. P. Norton, M. Inoue, and M. Yano, *Appl. Phys. Lett.* 86, 203105 (2005).
8. K. Wan, A. A. Porporati, G. Feng, H. Yang, and G. Pezzotti, *Appl. Phys. Lett.* 88, 251910 (2006).
9. B. Delley, *J. Chem. Phys.* 113, 7756 (2000), as implemented in BIOVIA Materials Studio platform.
10. E. B. Wilson, J. C. Decius, and P. C. Cross, *Molecular Vibrations*, Dover, New York, USA (1980).
11. T. Wermelinger, C. Borgia, C. Solenthaler, and R. Spolenak, *Acta Mater.* 55, 4657 (2007).
12. M. Kadleikova, J. Breza, and M. Vesely, *Microelec. J.* 32, 955 (2001).
13. O. Frank, G. Tsoukleri, J. Parthenios, K. Papagelis, I. Riaz, R. Jalil, K. S. Noveslov, and C. Galiotis, *ACS Nano* 4, 3131 (2010).
14. H. M. Oh, H. Jeong, G. H. Han, H. Kim, J. H. Kim, S. Y. Lee, S. Y. Jeong, S. Jeong, D. J. Park, K. K. Kim, Y. H. Lee, and M. S. Jeong, *ACS Nano* 10, 10446 (2016).
15. L. Yang, X. Cui, J. Zhang, K. Wang, M. Shen, S. Zeng, S. A. Dayeh, L. Feng, and B. Xiang, *Sci. Rep.* 4, 5649 (2014).
16. S. M. Lee, Y. H. Lee, Y. G. Hwang, J. R. Hahn, and H. Kang, *Phys. Rev. Lett.* 82, 217 (1999).
17. S. M. Lee, X. Kang, P. Wang, H. Cheng, and Y. H. Lee, *Chem. Phys. Chem.* 10, 1825 (2009).
18. D. L. Duong, G. H. Han, S. M. Lee, F. Gunes, E. S. Kim, S. T. Kim, H. Kim, Q. H. Ta, K. P. So, S. J. Yoon, S. J. Chae, Y. W. Jo, M. H. Park, S. H. Chae, S. C. Lim, J. Y. Choi, and Y. H. Lee, *Nature* 490, 235 (2012).
19. J. H. Kwak, J. Hu, D. Mei, C. W. Yi, D. H. Kim, C. H. F. Peden, L. F. Allard, and J. Szanyi, *Science* 325, 1670 (2009).
20. D. R. Lide, *Handbook of Chemistry and Physics*, 84th edn., CRC Press, Boca Raton, USA (2003).

Received: 12 August 2016. Accepted: 27 December 2016.